A Moment-Based Model of Multi-Site Emission for Porous Electrosprays

IEPC-2022-205

Presented at the 37th International Electric Propulsion Conference
Massachusetts Institute of Technology, Cambridge, MA, USA
June 19-23, 2022

Collin B. Whittaker[1], Joshua Eckels[2], Alex A. Gorodetsky[3] , and Benjamin A. Jorns[4]
University of Michigan, Ann Arbor, Michigan, 48109

A reduced fidelity model for the formation of and emission from multiple Taylor cone structures on a porous electrospray emitter is formulated. The model is predicated on balancing internal pressure against electrostatic pressure for a given location on the cone. The probability of multi-site emission is assessed by considering the porosity, cone dimensions, and distribution of applied electric field. There are five free parameters of the model, which are determined by applying the method of hierarchical Bayesian inference to an existing set of experimental measurements of number of emission sites and emitter current as a function of applied voltage. Subject to this inference, the model is found to reproduce the experimentally-observed behavior. It is found, however, that the inferred distribution of menisci properties disagrees with the properties of the substrate pores. This discrepancy is discussed within the context of possible propellant pooling.

I. Nomenclature

$f(p)$	=	unity-normalized pore/meniscus size distribution
p	=	pore/meniscus diameter
N_p	=	number of pores
ϕ	=	porosity
$\bar{A}_p$	=	mean pore area
$\mathrm{d}A$	=	area element
h	=	emitter height
R_c	=	emitter tip radius of curvature
α	=	emitter cone half-angle
d	=	electrode gap distance
R_A	=	aperture radius
s	=	arc length along emitter surface
$E(s)$	=	local electric field profile
N_s	=	number of active sites
1_O	=	onset criterion indicator function
$\bar{1}_O$	=	expected emission sites per pore
ε_0	=	vacuum permittivity
γ	=	propellant surface tension
α_0	=	capillary pressure onset coefficient
α_1	=	reservoir pressure onset coefficient

[1]PhD Candidate, Aerospace Engineering, cbwhitt@umich.edu
[2]PhD Candidate, Aerospace Engineering
[3]Assistant Professor, Aerospace Engineering
[4]Associate Professor, Aerospace Engineering

I = emitter current
i = site current
$\bar{i}$ = expected site per pore
K = propellant conductivity
$\hat{i}$ = dimensionless site current
ζ_0 = ionic emission offset
ζ_1 = ionic emission slope
$\hat{E}$ = dimensionless applied field
$\hat{E}_0$ = dimensionless onset field
$\hat{p_r}$ = dimensionless reservoir pressure
C_R = dimensionless hydraulic impedance
ρ = propellant density
$\left\langle \frac{q}{m} \right\rangle$ = beam charge to mass ratio
r_h = site hydraulic impedance
R_h = emitter hydraulic impedance
μ = propellant dynamic viscosity
κ = emitter substrate permeability
g_h = site hydraulic conductance
G_h = emitter hydraulic conductance
p_1 = pore size distribution lower bound
p_2 = pore size distribution upper bound
p^- = minimum permissible pore size
p^+ = maximum permissible pore size
N_d = number of data
X = collection of data
k = datum index
x = individual datum
V = emitter voltage
θ = collection of model parameters
$P(.)$ = probability
σ_{N_s} = number of sites datum noise
σ_I = current datum noise
F_{N_s} = model-predicted number of sites
F_I = model-predicted current
a_{N_s} = site data variance hyperparameter
a_I = current data variance hyperparameter
φ = collection of hyperparameters

II. Introduction

Electrosprays are an attractive method of producing energetic ion beams for space propulsive applications. Firstly, they operate on liquid propellants, which can be stored in compact form without need of pressurization, providing simplicity in storage and reducing risk (i.e. explosion hazards) to mission payloads. Secondly, electrospray propellants avoid the volume-to-area losses endemic to plasma-based electric propulsion (EP) technologies like gridded ion thrusters and Hall effect thrusters because the propellant (i.e. an ionic liquid) exists in a preionized state. Finally, the electrohydrodynamic and electrokinetic processes underpinning electrospray sources operate at the nanoscale, allowing individual electrosprays to produce thrust densities greater than that achieved by any other extant EP system, at least at the scale of individual emission sites [1].

Electrospray systems are chiefly limited, however, in that individual emitters produce small quantities of thrust, less than ~ 1 μN. To achieve thrust levels useful for tasks beyond fine attitude adjustment, it is necessary to aggregate hundreds or thousands of individual emitters together [2–4]. This introduces a key design challenge insofar as emitters can be manufactured only within finite tolerance, often significant on the scale of the device and possibly causing variability in performance [5]. Off-nominal behavior is potentially catastrophic to a fault-intolerant design [6], so it

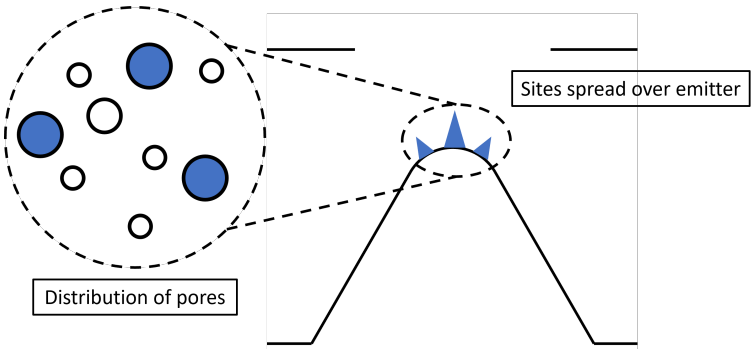

Fig. 1 Schematic representation of multi-site emission in a porous system

is highly desirable to predict device performance at comparatively small computational expense, such that one can consider the bulk performance of an array in light of this uncertainty.

The rich physics of electrospray emission make this prediction difficult. One particularly confounding process endemic to porous-type electrospray systems is multi-site emission, wherein a single electrospray emitter hosts multiple Taylor cone structures, each sustaining an independent beam of charge. This phenomenon has been well-observed experimentally [7–10], and indeed is a fundamental property of porous systems based on wedge-type geometries [11, 12]. It is potentially problematic, however, as it could lead to degraded device lifetimes. This is because if these additional beamlets result in substantial emission off the axis of thrust, they can lead to enhanced deposition of propellant on downstream electrodes, similar to when cone-jets bifurcate at high voltages in capillary-based systems [13]. Prediction of multi-site emission is then crucial to assessing how robust a potential emitter design is to failure.

As a result, previous efforts have sought to characterize multi-site emission through modeling. Wright *et al* considered the formation of multiple sites on porous wedge geometries and suggested it was the result of a periodic distribution in internal pressure [14]. This analysis explained how multiple sites could form on a wedge but it did not address the same problem for a porous conical geometry. Furthermore, St. Peter *et al* examined multi-site emission for conical-type emitters, using experimental data to form an empirical model[9]. Their hypothesis was that fluid would pool outside of substrate pores and gradually recede as voltage increased and additional sites developed. That said, there are two other potential mechanisms for the formation of multiple sites that have not been considered to date. The first is the porosity of the substrate, which exists as a population of pores of different sizes, each of which might host its own site and turn on at disparate voltages. This is somewhat similar to the St. Peter model, but was not explicitly treated there. The second is that the electric field at the emitter surface varies with position [5, 15], and so the onset and emission may differ over the finite area of the emitter. This lends itself to a new physical picture which tackles these additional mechanisms. The goal of this work, then, is to investigate these two phenomena rigorously.

Thus, we formulate a model for multi-site emission from an emitter of potentially arbitrary geometry and electric field distribution. The model proceeds as a successive hierarchy of moments over various predicted quantities, in this case the number of active emission sites and the emitter current. We then specialize the model to the case of porous conical-type electrosprays. To that end, this paper is organized in the following way. In Section III, we derive the model and the associated predictions for both the number of active sites on the emitter and the total current emitted by these sites; we similarly describe other constituent models and parameterize the geometry. To provide a validation case study for the model, in Sec. IV we then describe a hierarchical Bayesian inference problem to learn the associated model parameters from a set of training data in the literature. Finally, we present the results of the inference in Sec. V and discuss them in relation to the underlying physics and associated problem of predicting the performance of porous devices in Sec. VI.

III. Multi-Site Emission Model Framework

A. Model overview and emitter geometry

The fundamental construct of the model upon which other model predictions are predicated is that, by nature of the substrate, porous thrusters may host multiple electrospray emission sites (cf. [8, 9, 14]), and that these sites may be distributed over the body of the emitter. This is shown schematically in Fig. 1. We suppose that these emission sites are

localized to the surface pores of the substrate, whose distribution in size is described by some unity-normalized number density function $f(p)$, where p is the pore diameter, such that $f(p)\mathrm{d}p$ is the differential proportion of pores of class p. The assumption that potential emission sites are localized to surface pores can be relaxed and the distribution $f(p)$ interpreted more broadly as a distribution over meniscus sizes instead, which may be necessary to, for example, capture potential pooling phenomena [9]. We retain the terminology of pores as a visualization aid, and inasmuch as we might seek to predicate these predictions on a description of the substrate.

In this context, emission properties of interest, such as the number of active emission sites or the emitted current, can thus be described probabilistically as moments over this distribution, which results in an intensive quantity, a quantity per pore. Through proper scaling factors, this can be transformed into a quantity per area and integrated over the area of the emitter to determine the associated extensive quantity for the emitter. This description permits a description of position- and meniscus size- dependent behavior (e.g. a nonuniform electric field over the emitter).

The simplest of these moments is the following:

$$N_p = \iint f(p)\mathrm{d}p\frac{\phi}{\bar{A}_p}\mathrm{d}A, \tag{1}$$

where ϕ is the surface porosity of the substrate (the percent of the area occupied by pores), $\bar{A}_p = \int \frac{\pi}{4}p^2 f(p)\mathrm{d}p$ is the average pore area. In this case, the interior integral over p space is simply unity, and is the trivial intensive quantity — the number of pores per pore. When multiplied by $\frac{\phi}{\bar{A}_p}$, the number of pores per unit surface area, and integrated over the area of the emitter, this yields the total number of pores across the surface, N_p.

Some emission properties are functions of position-dependent quantities like the local electric field. It is useful, then, to parameterize the surface. In this work, we model emission from porous conical-type electrosprays, and as such we approximate the emitter as a spherically-capped cone. Under an assumption of axisymmetry, we choose the arc length s along the profile of the cone from its apex as a parameter, as illustrated in Fig. 2. Here, h is the height of the

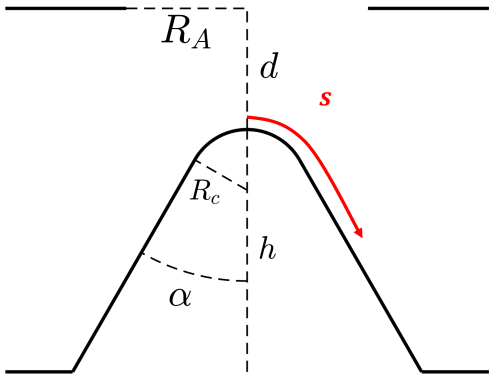

Fig. 2 Porous conical emitter geometry

emitter from its base to the tip of the spherical cap, R_c is the radius of curvature of the cap, α is the half-angle of the conical body, d is the distance between the the tip of the cap and the extractor, and R_A is the radius of the extractor aperture. The area element is discontinuous between the spherical cap and the cone body, and the mapping is thus given

$$\mathrm{d}A = \frac{\mathrm{d}A}{\mathrm{d}s}\mathrm{d}s, \tag{2}$$

$$\frac{\mathrm{d}A}{\mathrm{d}s} = \begin{cases} 2\pi R_c \sin\frac{s}{R_c}, & s \le (\frac{\pi}{2}-\alpha)R_c, \\ 2\pi\left[R_c\cos\alpha + \left(s - (\frac{\pi}{2}-\alpha)R_c\right)\sin\alpha\right], & s \in \left[\left(\frac{\pi}{2}-\alpha\right)R_c, \left(\frac{\pi}{2}-\alpha\right)R_c + \left(h - R_c\left(1-\sin\alpha\right)\sec\alpha\right)\right]. \end{cases} \tag{3}$$

Similarly, by the axisymmetry of the geometry, the electric field can be described as a function of s as well, $E = E(s)$. Emission properties of the emitter can then be described as integrals over $p - s$ space.

B. Onset criterion

The next highest moment determines the expected number of active emission sites on the emitter in a probabilistic sense, that is, those that have destabilized into Taylor cones. This is determined by invoking an indicator function of some onset criterion. The number of active emission sites is thus written as,

$$N_s = \iint 1_O(p, E(s))\, f(p)\mathrm{d}p \frac{\phi}{\bar{A}_p} \frac{\mathrm{d}A}{\mathrm{d}s}\mathrm{d}s. \tag{4}$$

The indicator function 1_O is a function of the pore size (via capillary pressure) and the local electric pressure, and takes a value unity when the onset criterion is satisfied and a value null otherwise. The interior integral $\bar{1}_O(E(s)) = \int 1_O(p, E(s))\, f(p)\mathrm{d}p$ is the mean number of emission sites per pore, which is strictly less than or equal to unity. In our case, we utilize an onset criterion of the form

$$1_O = \begin{cases} 1, & \sqrt{\frac{1}{2}\varepsilon_0}E(s) \geq \alpha_0\sqrt{\frac{4\gamma}{p}} - \alpha_1 p_r \left(\sqrt{\frac{4\gamma}{p}}\right)^{-1}, \\ 0, & \text{otherwise.} \end{cases} \tag{5}$$

Here, p_r is a reservoir pressure, which acts either to provide additional restoring force beyond the characteristic capillary force in the pore $\frac{4\gamma}{p}$, where γ is the fluid surface tension, or to provide additional positive pressure in excess of the electric pressure $\frac{1}{2}\varepsilon_0 E(s)^2$, which uses the vacuum permittivity ε_0. α_0 and α_1 are model parameters which capture the nontrivial dependence of the two restoring forces (cf. [16, 17]). Thus, this expression (for positive α_0, α_1) indicates that smaller pores (higher capillary pressures) increase the field required for onset, as do negatively-pressured reservoirs.

C. Current emission

The highest moment considered here yields the total current sourced by the emitter and is determined by integrating the current emitted by a site of a specified size and local electric field $i(p, E(s))$ over the active emission site density,

$$I = \iint i(p, E(s))\, 1_0(p, E(s))\, f(p)\mathrm{d}p \frac{\phi}{\bar{A}_p} \frac{\mathrm{d}A}{\mathrm{d}s}\, \mathrm{d}s. \tag{6}$$

The associated intensive quantity $\bar{i}(E(s)) = \int i(p, E(s))\, 1_O(p, E(s))\, f(p)\mathrm{d}p$ is the expected current per pore. Here, we assume the emitter is operating in a pure ionic regime (PIR), and so we invoke a simple scaling law for the current from a PIR emission site based on the numerical work of Coffman and later Gallud [16–18],

$$i = \frac{Kp^2}{4}\sqrt{\frac{8\gamma}{\varepsilon_0 p}}\max(\hat{i}, 0), \tag{7}$$

where K is the conductivity of the propellant,

$$\hat{i} = \frac{\zeta_0 + \zeta_1(\hat{E} - \hat{E}_0)}{C_R}, \tag{8}$$

$$\hat{E} = \frac{E(s)}{\sqrt{\frac{8\gamma}{\varepsilon_0 p}}}, \tag{9}$$

$$\hat{E_0} = \alpha_0 + \alpha_1 \hat{p}_r, \tag{10}$$

$$\hat{p}_r = \frac{p_r}{\frac{4\gamma}{p}}, \tag{11}$$

and

$$C_R = \frac{\frac{Kp^2}{4}\sqrt{\frac{8\gamma}{\varepsilon_0 p}}}{\frac{4\gamma}{p}\rho\left\langle\frac{q}{m}\right\rangle} r_h, \tag{12}$$

where ρ is the propellant density, $\left\langle \frac{q}{m} \right\rangle$ is the charge to mass ratio of the beam, Eq. (10) follows from (5), and r_h is the hydraulic impedance to the emission site, which is assumed to be related to the hydraulic impedance of the emitter R_h (cf. [7])

$$r_h = N_s R_h \tag{13}$$

$$= N_s \left(\frac{\mu}{2\pi\kappa} \frac{1}{1-\cos\alpha} \left[\frac{\tan\alpha}{R_c} - \frac{\cos\alpha}{h + R_c\,(\csc\alpha - 1)} \right] \right). \tag{14}$$

Here, μ is the dynamic viscosity of the propellant and κ is the absolute permeability of the substrate. Rigorously, Eq. (13) follows from the assumption that the hydraulic conductance of each emission site $g_h = \frac{1}{r_h}$ is equal, and that the conductance of the emitter $G_h = \frac{1}{R_h}$ is the sum of conductances to each site. Altogether, this model predicts that current emitted from the site is approximately linear in electric field about some dimensionless onset field $\hat{E}_0$, and is scaled by the hydraulic impedance, which results from a conductance-limited flow through the emitter geometry operating in the PIR.

D. Electrostatic field

The electric field distribution $E(s)$ is a generally nontrivial function of the emitter geometry that does not admit a simple analytical form. Consequently, to compute the mapping from the voltage applied to the emitter and the local electric field distribution over the emitter, we utilize a simple electrostatic solver that assumes the emitter surface is an equipotential (cf. [5]). The output of this simulation is the electric field magnitude at a finite number of locations, which can then be numerically integrated (i.e. by the trapezoidal rule) over s space.

E. Pore distribution

The pore distribution is also generally nontrivial and can be treated numerically in a similar manner. However, resolving such integrals over the combined $p - s$ space in sufficiently high resolution to eliminate significant integration error quickly becomes computationally expensive (~ 1 ms to evaluate, which is expensive if we seek to evaluate the model for an array of many thousands or tens of thousands of different emitters). To make this integral more analytically tractable, then, we assume a functional form for the pore distribution $f(p)$, namely

$$f(p) = \begin{cases} \frac{p_1 p_2}{p_2 - p_1} \frac{1}{p^2}, & p \in [p_1, p_2]\,, \\ 0, & \text{otherwise.} \end{cases} \tag{15}$$

This distribution uniformly distributes the pores in area space between some minimum pore size p_1 and some maximum pore size p_2, such that pores of each size will take up the same proportion of the area of the emitter. Practically, this distribution indicates that there will be a large number of smaller pores and a small population of large pores, as might be the case by agglomeration. Other similar distributions could be chosen in the same way and may have a modest effect on the exact model prediction; we have elected this distribution because it is comparatively uninformative (i.e. does not specify a particular pore size too stringently) and is eminently analytically tractable. The mean pore area of the distribution is

$$\bar{A}_p = \frac{\pi}{4} p_1 p_2. \tag{16}$$

It is generally the case that both $\bar{1}_O$ and $\bar{i}$ are still nontrivial to compute due to their discontinuous behavior (i.e. either on or off based on the onset criterion), such that the moments would have to be procedurally partitioned into the intervals for which the onset criterion is satisfied and the current prediction is positive. However, the onset criterion of Eq. 5 and the current model Eq. 7 each have at most two roots and their inflection is such that they are nonzero and continuous over at most a single interval, whose bounds we generically denote $[p^-, p^+]$. The needed integrals may be computed analytically over those intervals, where we note $[p^-, p^+]$ may be truncated by the closed pore distribution Eq. 15,

$$\bar{1}_O = \frac{p_1 p_2}{p_2 - p_1} \frac{p^+ - p^-}{p^- p^+}, \tag{17}$$

$$\bar{i} = \frac{\rho \langle q/m \rangle}{r_h} \frac{p_1 p_2}{p_2 - p_1} \left[2\gamma \left(\zeta_0 - \zeta_1 \alpha_0\right) \left(\frac{(p^+)^2 - (p^-)^2}{(p^+)^2 (p^-)^2} \right) + \frac{2}{3} \sqrt{2\gamma\varepsilon_0}\, \zeta_1 E(s) \left(\frac{(p^+)^{3/2} - (p^-)^{3/2}}{(p^+)^{3/2}(p^-)^{3/2}} \right) \right.$$
$$\left. + \zeta_1 \alpha_1 p_r \left(\frac{p^+ - p^-}{p^+ p^-} \right) \right]. \tag{18}$$

IV. Model Inference

We present now an inference problem over the model parameters of this multi-site emission model. The training data used are from a study by St. Peter *et al* of a single porous conical emitter operating on 1-ethyl-3-methylimidazolium-bis(trifluoromethylsulfonyl)imide (EMI-TFSI), for which individual beamlets, assumed to correspond to individual emission sites, were resolved with a micro-Faraday probe as a function of voltage and the associated emitter current measured [9]. We have thus a set of N_d data X, which we index $k = 1, 2, \ldots, N_d$, such that $X = \left\{x^{(k)}\right\} = \left\{x^{(1)}, x^{(2)}, \ldots, x^{(N_d)}\right\}$. Each datum is a current measurement and a count of the number of sites at a particular voltage, $x^{(k)} = \left(V^{(k)}, N_s^{(k)}, I^{(k)}\right)$, where the voltage data are taken as an independent variable.

While the multi-site emission model contains a large number of parameters that could be considered uncertain (see, for example, the analysis of [5]), here we examine only the model parameters ζ_0 and ζ_1, the parameters of $f(p)$, p_1 and p_2, and the surface porosity ϕ as uncertain. While in principle these latter three parameters could be predicated directly on properties of the substrate, there exists a nontrivial mapping between the volumetric pore structure of the substrate and its surface pore structure, and so we elect to learn them instead. Within the context of Bayesian inference, we seek to compute the posterior probability

$$\mathrm{P}(\theta \mid X) \propto \mathrm{P}(X \mid \theta)\ \mathrm{P}(\theta), \tag{19}$$

where $\theta = (\zeta_0, \zeta_1, p_1, p_2, \phi)$ is our set of learned parameters. The likelihood $\mathrm{P}(X \mid \theta)$ represents our degree of belief in the observed data given a set of model parameters (i.e. supposing the model was true), and is expressed practically as a noise model. Here, we choose for simplicity a Gaussian likelihood,

$$\mathrm{P}(X \mid \theta) = \prod_{k=1}^{N_d} \frac{1}{\sigma_{N_s}^{(k)}\sqrt{2\pi}} \exp\left[-\frac{\left(F_{N_s}\left(V^{(k)};\theta\right) - N_s^{(k)}\right)^2}{2\left(\sigma_{N_s}^{(k)}\right)^2} \right] \times \frac{1}{\sigma_I^{(k)}\sqrt{2\pi}} \exp\left[-\frac{\left(F_I\left(V^{(k)};\theta\right) - I^{(k)}\right)^2}{2\left(\sigma_I^{(k)}\right)^2} \right]. \tag{20}$$

Here, $F_{N_s}\left(V^{(k)};\theta\right)$ denotes the model-predicted number of sites at voltage $V^{(k)}$ as a function of parameters θ, $F_I\left(V^{(k)};\theta\right)$ is the similar model-predicted current, $\sigma_{N_s}^{(k)}$ is the standard deviation of noise in the k^{th} number of sites datum, and $\sigma_I^{(k)}$ is the same for the current datum. We have implicitly assumed here that the noise in each datum is independent.

The $\sigma_{N_s}^{(k)}$'s and $\sigma_I^{(k)}$'s, are often taken from experimentally-reported measurement uncertainty, which is not reported for the study in question, so rather than assign them arbitrarily, we have implemented here a hierarchical Bayesian inference scheme to learn the noise, subject to the assumed noise models

$$\sigma_{N_s}^{(k)} = \sigma_{N_s} = \sqrt{a_{N_s}}, \tag{21}$$
$$\sigma_I^{(k)} = \sigma_I = \sqrt{a_I}, \tag{22}$$

that is, the variance of the noise is a constant value for all data. The associated variances form the collection of hyperparameters $\varphi = (a_{N_s}, a_I)$, which me must learn alongside the data. This modifies Eq. (19) to be

$$\mathrm{P}(\theta, \varphi \mid X) \propto \mathrm{P}(X \mid \theta, \varphi)\ \mathrm{P}(\theta)\mathrm{P}(\varphi), \tag{23}$$

where we have assumed the prior distributions over θ and φ, $\mathrm{P}(\theta)$ and $\mathrm{P}(\varphi)$, to be independent. Thus, we must learn the noise alongside the parameters of actual interest.

As previously mentioned, all other parameters of the model we take to be certain, and we collect them in Tab. 1. The emitter geometries needed in Eqs. (3) and (14) and used to compute $E(s)$ with the electrostatic model were taken as quoted in [9]. The propellant properties, which appear in Eqs. 5, 7, 12, 14, and 18, are for EMI-TFSI, assume a

temperature of 295 K, and were calculated from the ESPET propellant database, a collection of ionic liquid physical and chemical properties built into the ESPET web app [9, 19]. The reservoir pressure of Eqs. 5, 11, and 18 was calculated as $-\frac{4\gamma}{p_r}$, where p_r is the largest pore radius in the reservoir, 40 μm for P3 grade, and the permeability estimated using data quoted for ROBU Glasfilter-GmbH's P5 frit, a provenance used elsewhere in [9]. The charge to mass ratio of Eqs. 12 and 18 is estimated from the data of [20], also quoted in [9], for 1516 V operation of another porous ionic electrospray emitter operation on EMI-TFSI for which time-of-flight spectroscopy data is available. As a simplifcation, all current content that arrives after the nominal arrival time of trimer cations is assumed to also be composed of trimer species. Finally, the coefficients for the onset criterion α_0 and α_1, which appear in Eqs. 5, 10, and 18, were fit to numerical simulation results presented by Coffmann *et al* [16] for individual emission sites, which show a strongly linear dependence of the onset field $\hat{E}_0$ with reservoir pressure $\hat{p}_r$. Interestingly, even for no reservoir pressure, these results predict that Taylor cone-like structures can begin to form at electric fields nearly a factor of two lower than might be calculated by directly equating the electric pressure to the characteristic capillary pressure in the pore, for which the corresponding parameter would be $\alpha_0 = 1$.

Parameter	Value	Units
R_c	1.6×10^{-5}	m
d	1.2×10^{-4}	m
R_A	7.5×10^{-4}	m
α	30	deg
h	3.5×10^{-4}	m
K	7.345×10^{-1}	S m^{-1}
γ	3.511×10^{-2}	N m^{-1}
ρ	1522	kg m^{-3}
μ	3.394×10^{-2}	Pa-s
p_r	-3511	Pa
κ	1.51×10^{-13}	m^{-2}
$\left\langle \frac{q}{m} \right\rangle$	3.29×10^{5}	C kg^{-1}
α_0	5.19×10^{-1}	unitless
α_1	4.00×10^{-1}	unitless

Table 1 Model parameters Treated as certain for this analysis and their respective values

Finally, Tab. 2 specifies the prior distributions used in the inference. Each was chosen to be comparatively uninformative, usually only enforcing the sign of a quantity. Furthermore, prior distributions over parameters are assumed independent. With these, the inference problem is now fully specified.

Parameter	Distribution	Units
ζ_0	$\mathcal{U}(-\infty, \infty)$	unitless
ζ_1	$\mathcal{U}[0, \infty)$	unitless
p_1	$\mathcal{U}[0, \infty)$	m
p_2	$\mathcal{U}[0, \infty)$	m
ϕ	$\mathcal{U}[0, 1]$	unitless
a_{N_s}	$\mathcal{U}[0, \infty)$	unitless
a_I	$\mathcal{U}[0, \infty)$	A^2

Table 2 Prior distribution over parameters θ and hyperparameters φ

V. Results

A. Posterior parameter distributions

We drew 10^6 samples from the posterior distribution using a Markov-chain Monte Carlo sampling algorithm (cf. [5]). We show a corner plot of the corresponding samples in Fig. 3. The intervals over which the corner plot data is

shown are given in Tab. 3, along with the parameter sample mean and sample standard deviation. As evident in the figure, the parameters and hyperparameters are largely uncorrelated with each other. Notable exception, however, is found between ζ_0 and ζ_1, which show a comparatively strong negative correlation, and to a lesser degree between ζ_1 and p_1 and p_2 and ϕ. Additionally, most all parameters have a unimodal distribution with some characteristic width, except ζ_0, which has two peaks, one around -.00368 and one around -.00296, and ϕ, which has one peak at around .934 and one pushing to the boundary at 1. Lastly, we note that the value of ionic emission slope learned here agrees within a factor of two with that learned for a similar model on a different system of similar architecture operating on a different propellant (cf. the ζ_2 of [5]). This provides evidence to support the claim that the parameter ζ_1 should be a universal property of purely ionic electrosprays, regardless of propellant or device geometry (cf. [18]).

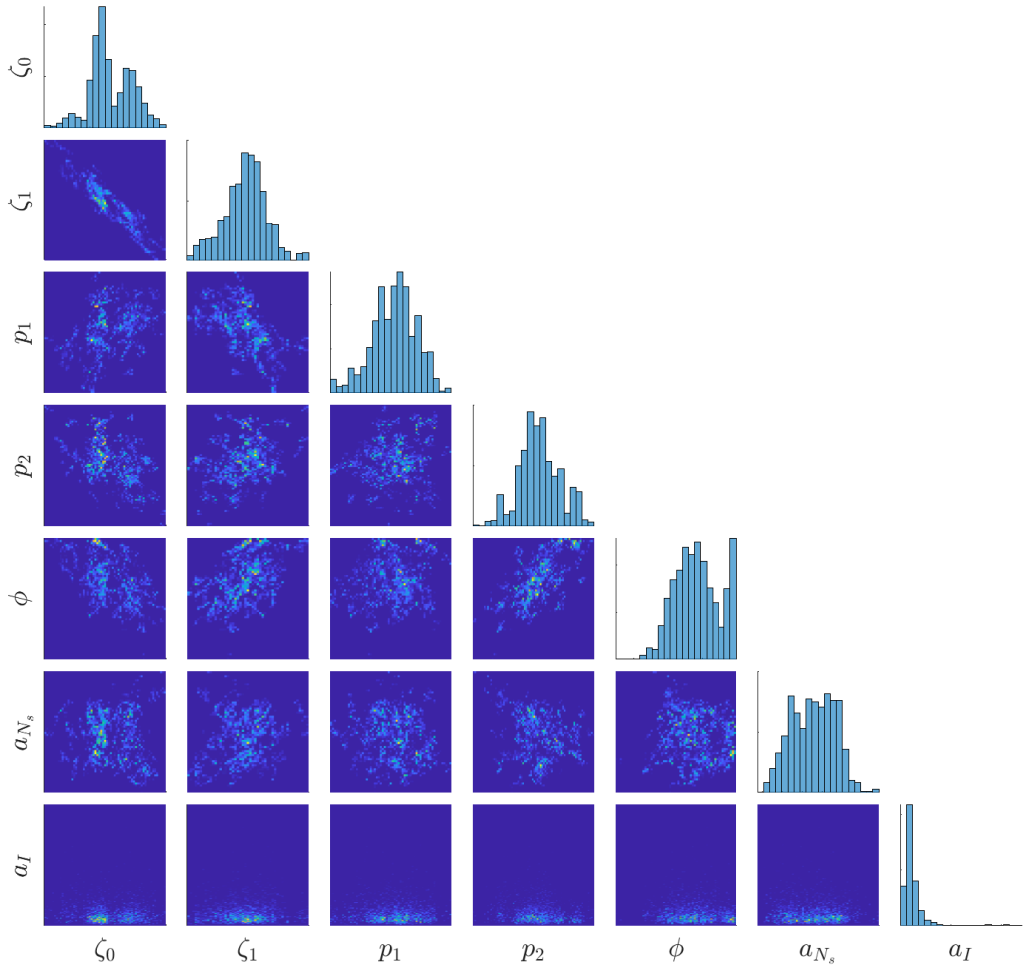

Fig. 3 Corner plot for the 10^6 samples drawn from the posterior distribution; the structure of the plot mimics a covariance matrix, with the diagonal entries being the marginal histograms for each parameter or hyperparameter, and the off-diagonal entries being 2-d histograms of the corresponding 2-d subspace; limits for the histogram domains are shown in Tab. 3

Parameter	Sample Mean	Sample Standard Deviation	Corner Plot Limits	Units
ζ_0	-3.45×10^{-3}	5.56×10^{-4}	$\left[-5.15 \times 10^{-3}, -2.00 \times 10^{-3}\right]$	unitless
ζ_1	5.19×10^{-2}	2.60×10^{-3}	$\left[4.50 \times 10^{-2}, 5.97 \times 10^{-2}\right]$	unitless
p_1	3.85×10^{-6}	3.35×10^{-7}	$\left[2.88 \times 10^{-6}, 4.71 \times 10^{-6}\right]$	m
p_2	2.04×10^{-5}	1.28×10^{-6}	$\left[1.62 \times 10^{-5}, 2.38 \times 10^{-5}\right]$	m
ϕ	9.43×10^{-1}	3.26×10^{-2}	$\left[8.25 \times 10^{-1}, 1.00 \times 10^{0}\right]$	unitless
a_{N_s}	7.13×10^{-1}	2.16×10^{-1}	$\left[1.60 \times 10^{-1}, 1.36 \times 10^{0}\right]$	unitless
a_I	4.45×10^{-14}	2.78×10^{-14}	$\left[0, 4.80 \times 10^{-13}\right]$	A^2

Table 3 Sample mean and sample standard deviation for the posterior, and domain limits for Fig. 3

B. Posterior predictions

We also collect in Figs. 4 and 5 posterior predictions for the number of sites and current, respectively, over the domain of the training data. In both cases, the median prediction, and the population of predictions more broadly,

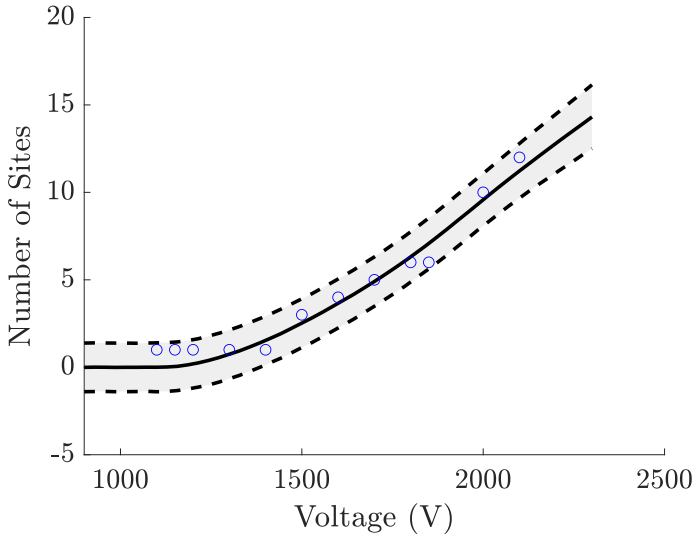

Fig. 4 Posterior predictions for the number of active sites; the data of [9] are shown as blue circles, the solid black line is the median prediction over the domain, and the shaded area within the dashed black lines contains 90% of the posterior predicted probability

tracks well the experimental data. In particular, the model is successful in replicating that at low voltages, there may be only a single emission site observable on the emitter, but that as the voltage increases, many more sites are observed (for the training data, there is only one resolvable beamlet below 1500 V, but over 10 distinct beamlets above 2000 V). Noticeably, the model is positively inflected below about 1900 V, but becomes slightly negatively inflected thereafter; this is indicative of a potential saturation in the number of possible sites. For the current predictions, the model is similarly well capable of reproducing the experimentally observed behavior, including the tenuous current sourced in the low-voltage regime and the current more strongly increasing with voltage thereafter. In accordance with the experimental data, the predicted current is largely linear with voltage in the moderate voltage regime, though the predicted current becomes positively inflected again at the edge of the experimental domain. This is interesting for its divergence with the predicted number of sites, which behave similarly in the other regimes. This suggests that the onset of multiple sites serves to modulate the emitted current, but that once the number of sites begins to saturate in this higher-voltage regime, the current begins to scale differently. Lastly, we observe that the envelope of our predictions encloses most of the experimentally observed data, as we might presume, since we learned them as part of our hierarchical inference problem.

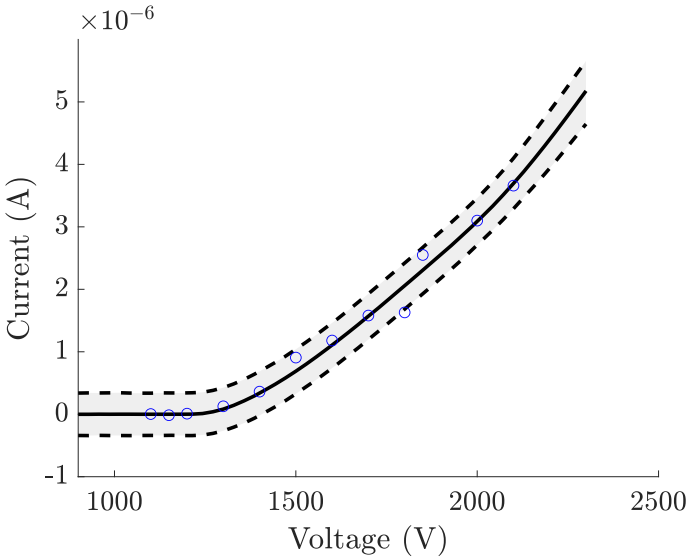

Fig. 5 Posterior predictions for the current; the data of [9] are shown as blue circles, the solid black line is the median prediction over the domain, and the shaded area within the dashed black lines contains 90% of the posterior predicted probability

VI. Discussion

A. Near-onset regime physics

The fact that the ionic emission offset and slope parameters ζ_0 and ζ_1 of Eqs. 7 and 18 are strongly correlated is initially surprising. While it is intuitively straightforward that this might be the case if we imagine trying to fit a line to a single datum (i.e. an underdetermined system), we would anticipate that given the range of voltage data incorporated into the inference we should be able to discriminate between them. This correlation, then, likely results because the slope ζ_1 also modulates the reduction in current associated with the onset field $\hat{E}_0$, which is not itself a function of voltage. Since for larger electric fields the ζ_0 term becomes small on the scale of the ζ_1 term, ζ_0 serves primarily to modulate the current in the tenuous emission regime close to the first onset of spray. Its negative value here means that in a small region just beyond onset, the site is predicted not to emit any current, which is likely a consequence of the richer physics ignored in the linearization to obtain Eq. 8.

B. Model predictions as expectations

Relatedly, through this modulation the model is successful in reproducing the current emission in this near-onset regime, it noticeably underpredicts the number of emission sites. This incongruity results, in part, because the form of our model prediction and the data are not exactly the same. The data is some discrete count of the number of emission sites (as determined by some number of beamlets). However, within this moment-based construction the model prediction is an expectation, that is, an average number of sites; for example, this is why the model prediction is not necessarily a whole number. Through a frequentist lens, we could intuit this as meaning that if we had many emitters, each of which described by the same distribution in p-s space, we would expect that as a result of the random nature of the substrate, some may have emission sites in this near-field regime and some may not. In this way, this formulation admits some kind of variance, which for the analysis considered here has been partially captured by the learned hyperparameter a_{N_s}, which despite the simplicity of the noise model has placed the data largely within the associated credible interval. To capture this stochastic behavior more rigorously, one could interrogate the variance in the model prediction itself through higher moments over the distribution or by sampling from the associated site density over p-s space.

C. Correspondence with substrate properties

Finally, we reflect on the learned surface pore properties, p_1, p_2, and ϕ. It is evident that the associated pore sizes are larger than might be directly assumed from the nominal properties of the substrate. That is, for P5 frit, the largest internal pore size is approximately 1.6 μm, but the posterior places the distribution of surface pores between about 4 and 20 microns in diameter. This mismatch is not necessarily surprising, inasmuch as the internal pore sizing reflects that, among the many tortuous paths that pass through the substrate, each narrows to 1.6 μm at some point, but may be larger in other segments. Given the highly isotropic nature of the substrate, which is composed of many small particles that are sintered together, we anticipate the characteristic length of such paths to be not much larger than the characteristic size of the pores themselves, And so indeed on the scale of the device we should expect to see surface pores of concomitant size to the internal pores.

This mapping, however, is complicated further by two effects. Firstly, the substrate was, by consequence of the emitter's manufacture, subject to some abrasive process which could change the local substrate properties through the fracture or wholesale removal of particles, creating larger voids. Secondly, the interfacial phenomena which control the equilibrium position of the meniscus are complex and in principle may depend on the electric field as it acts to change the local balance of stresses. Correspondingly, taking the relaxed interpretation that the distribution $f(p)$ and the associated porosity ϕ are a description over menisci instead of strictly pores, these results then suggest that there may exist a nonnegligible pooling effect of the propellant, as has been considered previously [9, 21, 22]. The clearest potential indication of such an effect here is the learned porosity, which with a mean value of 0.943 is substantially larger than the associated volumetric porosity of the substrate, around 0.5, indicating that much more of the surface may be taken up by menisci than is purely by void area. In principle, this effect is voltage-dependent to where we could parameterize the meniscus size distribution as $f(p; E(s))$; however, a stationary distribution as implemented here may still be a decent approximation, since it is usually the largest sites that are predicted to activate first, and thus pooling to larger menisci likely precedes significant emission, at least in part.

VII. Conclusion

We have expounded a framework for modeling multi-site emission in porous electrosprays as moments over menisci size and space. We then fit this to a set of training data by learning its associated model parameters through a hierarchical Bayesian inference scheme, and insodoing were able to replicate the experimentally observed behavior, a positive indicator for the model's potential predictive capability. In examining the corresponding inference results, we have been able to interrogate associated physics, in particular both indicating that a more robust description of device behavior is warranted in the tenuously emitting near-onset regime and providing indirect evidence of pooling or a similar phenomenon on the emitter. Moving forward, this model opens new possibilities for predictive modeling of electrospray arrays. In particular, this tool, when coupled with an associated model for beamlet divergence, could be used to predict the distribution of the emitter current in space in addition to the total emitted current. Furthermore, expanding the model predictions to treat both the expected model quantities and the variance in those quantities could be used to treat the inherent randomness of the emission process. Such an architecture ultimately endorses incorporation of this model into a robust design problem for electrospray emitters that seeks to maximize device lifetimes by identifying devices that maintain desirable performance even under uncertainty in behavior and manufacturing.

Acknowledgements

This work was supported by an Early Stage Innovations grant from NASA's Space Technology Research Grants Program, and by a NASA Space Technology Graduate Research Opportunity (80NSSC21K1247). The authors wish to thank Mr. Benjamin St. Peter and Drs. Rainer Dressler and John Yim for their many useful discussions.

References

[1] Lozano, P. C., Wardle, B. L., Moloney, P., and Rawal, S., "Nanoengineered thrusters for the next giant leap in space exploration," *MRS Bulletin*, Vol. 40, No. 10, 2015, p. 842–849.

[2] Natisin, M. R., Zamora, H. L., McGehee, W. A., Arnold, N. I., Holley, Z. A., Holmes, M. R., and Eckhardt, D., "Fabrication and characterization of a full conventionally machined high-performance porous-media electrospray thruster," *Journal of Micromechanics and Microengineering*, Vol. 30, 2020, p. 115021.

[3] Legge, R. S., and Lozano, P. C., "Electrospray Propulsion Based on Emitters Microfabricated in Porous Metals," *Journal of Propulsion and Power*, Vol. 27, No. 2, 2011, pp. 485–495.

[4] Krejci, D., Mier-Hicks, F., Fucetola, C., Lozano, P., Schouten, A. H., and Martel, F., "Design and Characterization of a Scalable Ion Electrospray Propulsion System," *International Electric Propulsion Conference*, 2015, p. 149.

[5] Whittaker, C. B., Gorodetsky, A. A., and Jorns, B. A., "Model Inference on an Electrospray Thruster Array," *AIAA 2022 SciTech Forum*, 2022, p. 0041.

[6] Jorns, B. A., Gorodetsky, A., Lasky, I., Kimber, A., and Dahl, P., "Uncertainty Quantification of Electrospray Thruster Array Lifetime," *International Electric Propulsion Conference*, 2019, p. 317.

[7] Courtney, D. G., "Ionic Liquid Ion Source Emitter Arrays Fabricated on Bulk Porous Substrates for Spacecraft Propulsion," Ph.D. thesis, Massachusetts Institute of Technology, 2011.

[8] Perez-Martinez, C., and Lozano, P., "Ion field-evaporation from ionic liquids infusing carbon xerogel microtips," *Applied Physics Letters*, Vol. 107, No. 4, 2015, p. 043501.

[9] St.Peter, B., Dressler, R. A., Chiu, Y.-H., and Fedkiw, T., "Electrospray Propulsion Engineering Toolkit (ESPET)," *Aerospace*, Vol. 7, No. 91, 2020.

[10] Fedkiw, T. P., Wood, Z. D., and Demmons, N., "Improved Computed Tomography Current Mapping of Electrospray Thrusters," *AIAA Propulsion and Energy 2021 Forum*, 2021, p. 3389.

[11] Courtney, D. G., and Shea, H., "Influences of porous reservoir Laplace pressure on emissions from passively fed ionic liquid electrospray sources," *Applied Physics Letters*, Vol. 107, 2015, p. 103504.

[12] Courtney, D. G., Alvarez, N., and Demmons, N., "Electrospray Thrusters for Small Spacecraft Control: Pulsed and Steady State Operation," *2018 Joint Propulsion Conference*, 2018, p. 4634.

[13] Wright, P. L., Thuppul, A., and Wirz, R. E., "Lift-Limiting Emission Modes for Electrospray Thrusters," *2018 Joint Propulsion Conference*, 2018, p. 4726.

[14] Wright, P. L., and Wirz, R. E., "Multiplexed electrospray emission on a porous wedge," *Physics of Fluids*, Vol. 33, 2021, p. 012003.

[15] Eckels, J. D., Whittaker, C. B., Jorns, B. A., Gorodetsky, A. A., St.Peter, B., and Dressler, R. A., "Simulation-based surrogate methodology of electric field for electrospray emitter geometry design and uncertainty quantification," *37th International Electric Propulsion Conference*, 2022, p. 271.

[16] Coffman, C. S., Martínez-Sánchez, M., and Lozano, P. C., "Electrohydrodynamics of an ionic liquid meniscus during evaporation of ions in a regime of high electric field," *Physical Review E*, Vol. 99, 2019, p. 063108.

[17] Gallud, X., and Lozano, P. C., "The emission properties, structure and stability of ionic liquid menisci undergoing electrically assisted ion evaporation," *Journal of Fluid Mechanics*, Vol. 933, 2022, p. A43.

[18] Coffman, C., Martinez-Sanchez, M., Higuera, F., and Lozano, P. C., "Structure of the menisci of leaky dielectric liquids during electrically-assisted evaporation of ions," *Applied Physics Letters*, Vol. 109, No. 23, 2016, p. 231602.

[19] St. Peter, B., and Dressler, R., "ESPET Web App," , 2022. URL `http://espet.spectral.com/`.

[20] Perez-Martinez, C. S., "Engineering ionic liquid ion sources for ion beam applications," Ph.D. thesis, Massachusetts Institute of Technology, 2016.

[21] Wright, P. L., and Wirz, R. E., "Transient FLow in Porous Electrospray Emitters," *AIAA Propuslion and Energy 2021 Forum*, 2021, p. 3437.

[22] Gallud-Cidoncha, X., Kristinsson, B. O., and Lozano, P. C., "Informing the Design of Pure-ion Electrospray Thrusters via Simulation of the Leaky-Dielectric Model with Charge Evaporation," *36th International Electric Propulsion Conference*, 2019, p. 610.